Contents of this file

- 1. Text S1: Description of DEM Construction
- 2. Text S2: Description of model sensitivity
- 3. Table S1

5

4. Figures S1 to S6

Introduction This supporting information provides method description of the DG-IS2- DEM and a discussion of model sensitivity. Figures showing velocity observations and simulations from downstream to upstream regions for all the five glaciers, and additional figures mentioned in the main article.

1 DG-IS2-DEM Construction

The DG-IS2-DEMs are constructed using software derived from the algorithms that generate the ICESat-2 ATL14 (global landice DEM) and ATL15 (global land-ice height change) products, with modifications to allow elevation-change solutions that 1) use the higher resolution (40-m) ATL06 product (Smith et al., 2023a) instead of the lower resolution (120-m) ATL11 (Smith et al., 2021) products from ICESat-2; 2) include both ICESat-2 data and DEM data from the Polar Geospatial Center archive of Worldview-derived DEMs (Porter et al., 2022) and; 3) correct for surface-elevation variations due to SMB and firn-air-content variability.

Like the ATL14/15 algorithm, the algorithm used here matches elevation data with model elevations (z_m) of the form:

$$z_m = z_0(x, y) + \delta z(x, y, t) + z_b(i, x, y) + \delta h_a(x, y, t)$$
(1)

where x and y are the data coordinates, t is the time of data acquisition, and i is an index parameter that distinguishes different groups of data (i.e. data from different beams and different orbits of ICESat-2 acquisition, or different Worldview DEMs). The model is parameterized as a DEM for a specific reference time, $z_0(x,y)$, an elevation-change field $\delta z(x,y,t)$, and a set of bias estimates, $z_b(i,x,y)$, and δh_a is an estimate of the air content in the firn, derived from a firn-densification model (Medley et al., 2022). The DEM has a resolution of 50 m, and the elevation-change field has a horizontal resolution of 400 m and a temporal resolution of 0.25 yr, and model elevations are calculated by linear interpolation into the corresponding model component.

We determine the model parameters by minimizing a combination of the mismatch between the model elevations and sparse observations of surface elevation and the complexity of the model itself. Our solution minimizes an approximation of the quantity:

$$R^2 = E_{data}^2 + C_{z0}^2 + C_{\delta z}^2 + C_{bias}^2 \tag{2}$$

where E_{data}^2 is the data-model misfit, C_{z0}^2 is a measure of the complexity of the DEM, $C_{\delta z}^2$ is a measure of the elevation changes, and C_{bias}^2 is a measure of the complexity of the bias estimates. We describe each in turn.

The data-model misfit, E_{data}^2 , is just the sum of the squared differences between measured elevations and model elevations, divided by their estimated errors:

$$E_{data}^2 = \sum_{data} \frac{(z_d - z_m)^2}{\sigma_d^2} \tag{3}$$

The DEM complexity, C_{z0}^2 , is equal to a weighted sum of the integrals of its squared first and second derivatives:

$$C_{z0}^2 = \iint \frac{1}{\sigma_{xx}^2} \left[\left(\frac{\partial^2 z_0}{\partial x^2} \right)^2 + 2 \left(\frac{\partial^2 z_0}{\partial x \partial y} \right)^2 + \left(\frac{\partial^2 z_0}{\partial y^2} \right)^2 + \frac{1}{L^2} \left[\left(\frac{\partial z_0}{\partial x} \right)^2 + \left(\frac{\partial z_0}{\partial y} \right)^2 \right] \right] dA$$
 (4)

We have found that choosing a value of L equal to the largest expected spatial gap between measurements helps suppress excessive extrapolation of data values into data gaps; based on the density of ICEsat-2 values, we set L equal to 1 km.

The complexity of the elevation-change field is the sum of the integrals of the squared first and second derivatives of the rate of elevation change and the integral of the second derivative of the elevation-change rate:

$$C_{\delta z}^{2} = \iiint \left[\frac{1}{\sigma_{xxt}^{2}} \left[\left(\frac{\partial^{2} \delta z_{t}}{\partial x^{2}} \right)^{2} + 2 \left(\frac{\partial^{2} \delta z_{t}}{\partial x \partial y} \right)^{2} + \left(\frac{\partial^{2} \delta z_{t}}{\partial y^{2}} \right)^{2} \right. \\ \left. + \frac{1}{L^{2}} \left[\left(\frac{\partial \delta z_{t}}{\partial x} \right)^{2} + \left(\frac{\partial \delta z_{t}}{\partial y} \right)^{2} \right] \right] + \frac{1}{\sigma_{tt}^{2}} \left(\frac{\partial^{2} \delta z_{t}}{\partial^{2} t} \right) \right] dAdt$$

$$(5)$$

40

45

55

The bias model is made up of (1) a distinct bias estimate for each distinct beam pair in the ICESat-2 data (i.e. for each pair of beams in each repeat track and each cycle) (2) a distinct mean bias for each DEM, and (3) a distinct grid of spatially varying biases for each DEM with a resolution of 2500 m. The complexity of the DEM bias model is then:

$$C_{bias}^{2} = \sum_{ICESat-2} \frac{b_{TP}^{2}}{\sigma_{TP}^{2}} + \sum_{DEMs} \left[\frac{\delta z_{DEM0}^{2}}{\sigma_{DEM0}} + \iint \frac{1}{\sigma_{\delta z_{DEM}}^{2}} \delta z_{DEM}^{2} dA + \iint \frac{1}{\sigma_{\nabla DEM}^{2}} \left(\frac{\partial \delta z_{DEM}^{2}}{\partial x} + \frac{\partial \delta z_{DEM}^{2}}{\partial y} \right) dA \right]$$

$$(6)$$

The complexity for the spatially varying biases for each DEM is the squared integral of the bias values plus the squared integral of its gradient.

The equations for the complexity values include scaling parameters that determine the importance of each component $(\sigma_{xx}^2, \sigma_{xxt}^2, \sigma_{tt}^2, \sigma_{\delta zDEM}^2)$, and $\sigma_{\nabla DEM}^2$. These are effectively tuning parameters that allow adjustment of the final result: increasing them produces a solution that is more faithful to the data, but may be rougher and contain more of the data artifacts, while reducing them produces a smoother solution that may ignore real features in the data. We selected these parameters using a combination of manual tuning and parameter choices derived using mode quantitative methods for the ICESat-2 ATL14 and ATL15 products (Smith et al., 2023b), and are as follows:

 $\begin{array}{lll} \sigma_{xx} & 0.03 & \text{Suppress small-scale DEM artifacts (derived from ATL14)} \\ \sigma_{xxt} & 0.001 \ yr^{-1/2} & \text{Segregate elevation changes in lakes from background 0.01} \\ \sigma_{tt} & 12000 \ myr^{-3/2} & \text{Avoid poorly conditioned solutions} \\ \sigma_{\delta z_{DEM}}^2 & 1m^2 & \text{Allow DEM bias grids to capture short-wavelength DEM errors} \\ \sigma_{\nabla DEM}^2 & 0.0006 \ m & \text{Limit the large-scale slope of DEM grid biases} \\ \end{array}$

Note that the units of the constraint parameters are chosen so that each term in (2) is unitless, which implies that each parameter in (5) has units of $[value][A]^{1/2}$, and each parameter in (6) has units of $[value][AT]^{1/2}$ where value is the quantity being constrained, A is area, and T is time.

The procedure to solve for grids of values that minimize (2) is similar to that used to construct the ICESat-2 ATL14/15 product (Smith et al., 2023b): We divide the solution domain into 20×20 -km tiles that overlap their neighbors by 10 km. For each tile, we construct systems of equations that describe the linear interpolation between the elevation grids and the data values (1), and that describe the constraint equations (4-6), and using a QR-transform of the matrix of coefficients that describes the equations to solve for the optimal grid-elevation and bias values. To help minimize the effects of data points with large errors in the solutions, we iterate the solution: After each iteration we calculate error-scaled residuals between the data and the best-fitting grids, estimate the geophysical noise in the data (i.e. the error not captured by the per-data-point error estimates) and eliminate any data points with scaled residuals that are larger than three times the robust spread. We then recalculate the

least-squares solution; these iterations may be repeated up to six times. After calculating a solution for each tile, we construct a mosaic of the elevations and elevation changes from all of the tiles, smoothly blending values between adjacent tiles.

Figure S1 shows the results of the DEM-estimation process for the region between EQP and AVA. Panel (a) shows the shaded-relief DEM derived from the combination of ICESat-2 and DEM data, and panel (b) shows the mean recovered elevation-change rate between mid 2019 and mid 2022. The largest change rates are focused on at the termini of KAN, KUJ, and EQP, with minor thickening in the downstream part of AVA. Panel (c) shows the RMS of elevation values from all input data, collected into 250-m grid cell. The dominant signal in most grid cells is related to the slope of DEM (compare with (a)); calculating the RMS elevation after subtracting the DEM (panel (d)) shows that the next-most-significant signal is related to biases in the input DEM data, which is manifest in this plot as rectangular areas of enhanced variance that follow the boundaries of individual DEMs. Subtracting elevation-change and bias signals leaves much smaller residuals (panel (e)) that appear to be most strongly related to the extent of crevassing in the lower parts of the glaciers.

2 Model sensitivity and derived stress coupling lengths

80

90

We re-run our terminus driven model for each glacier at a set of locations (blue points in Figure 1) that span up and downstream from our original choice of location (red points in Figure 1). This is done for two reasons. First, we aim to test the robustness of the terminus driven model results when the the location of the simulated velocity is shifted. Second, we wish to quantify the spatial decay of the seasonal velocity perturbation away from the terminus. For KUJ and EQP, velocities closest to the terminus are highest in magnitude and decay with distance from the terminus, although the general temporal pattern in velocity observations is preserved further upstream (Figures S3 and S5). For AVA and KAN the velocity pattern upstream from the terminus is only subtly different than that at the terminus (Figures S2 and S4). This is consistent with the idea that terminus-driven velocity change will be primarily concentrated close to the terminus and our earlier result that AVA and KAN are not terminus-controlled.

Simulated velocities do not decay as the distance from the terminus increases at the same rate as the observed velocity, particularly for KUJ, where we overestimate the velocity in the upstream regions in 2017 and 2020 and underestimate the velocity in 2021 (Figure S3e and f). This suggests that there may be factors other than terminus change that occasionally influence the seasonal velocity for KUJ. For EQP, we see a greater difference between the simulated velocities with fixed and varying elevation (Figure S5). For this glacier adding changes in elevation produced more accurate predictions further upstream while overestimating velocity further downstream. We hypothesize that seasonal elevation change of EQP acts to dampen the seasonal velocity signal in the upstream region, potentially propagating downstream. However, since the terminus-driven model only considers the geometry at a given location, it thus fails to capture such propagation.

Felikson et al. (2017) and Felikson et al., (2021) quantified the Péclet number (Pe) of our studied glaciers. Most of the dynamic mass loss occurs downstream of Pe = 3 (Felikson et al., 2021). Pe=3 locations for these glaciers are KAN = 32 km; AVA = 27 km; KUJ = 28 km; and EQP = 15 km (Felikson et al., 2021). The stress coupling lengths chosen based on minimizing the difference between observed and modeled velocity are EQP = 10 km and KUJ = 20 km. These are shorter than the Pe = 3 location. Our estimation of stress coupling length might be uncertain since we assume a constant stress coupling length along the profile and the terminus-driven model is a simplified 1-D model.

Table S1. The mean relative difference between velocity simulations and observation using different stress coupling lengths.

Length (m) Glacier name	8000	10000	15000	20000	25000
EQP	7.1%	6.2%	6.3%	6.9%	7.5%
KUJ	11.1%	8.4%	5.4%	5.0%	5.1%
KAN	14.5%	13.4%	12.4%	12.1 %	12.0%
AVA	65.0%	64.4%	63.7%	63.2 %	63.1%

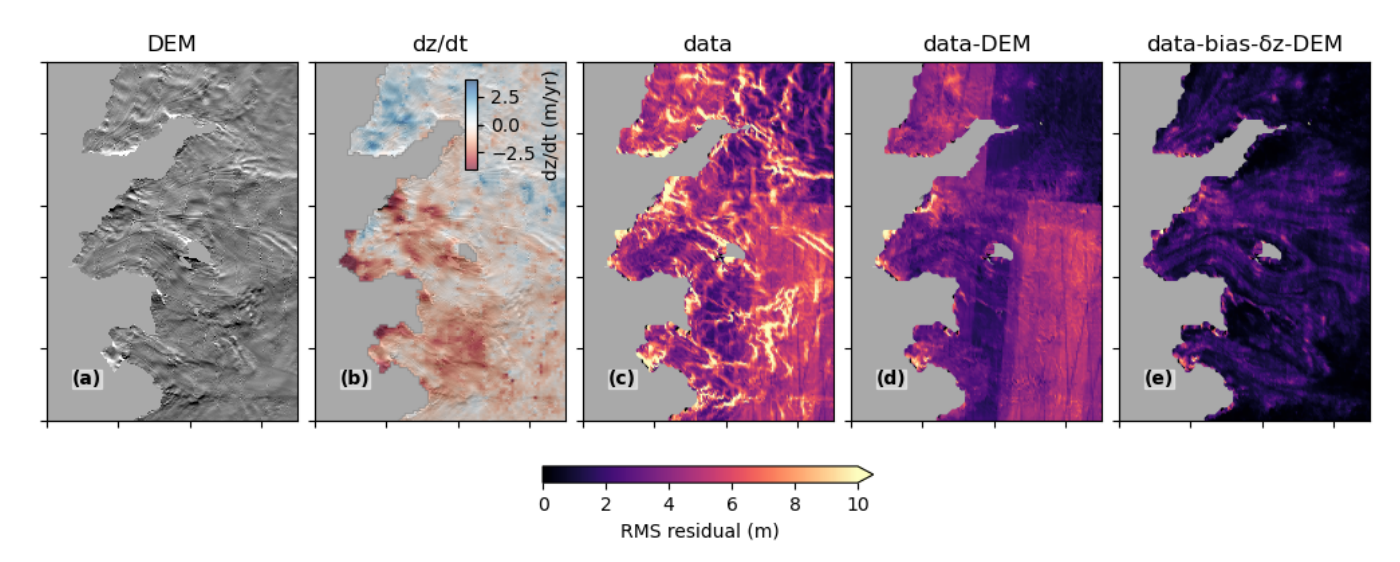


Figure S1. Panels show: (a): shaded-relief image of the 2021 DEM of the EQP-AVA glaciers, (b): elevation-change rate between June of 2019 and June of 2022, (c):RMS of elevation values in 250-meter grid cells, (d):RMS of elevation values corrected for the DEM, (e): RMS of elevation values corrected for the DEM, sensor-to-sensor biases, and elevation change.

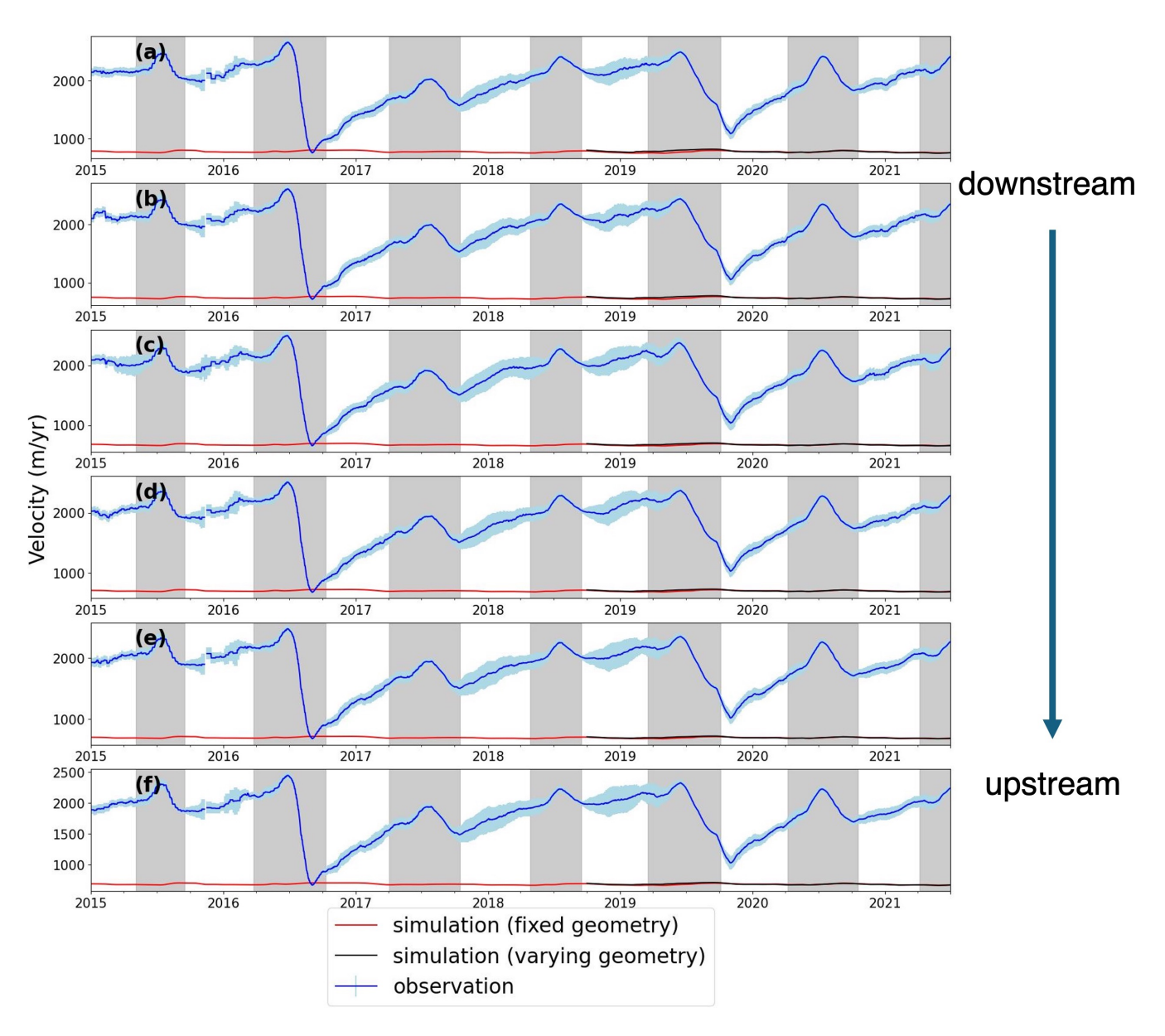


Figure S2. Velocity observations and simulations from downstream to upstream regions for AVA.

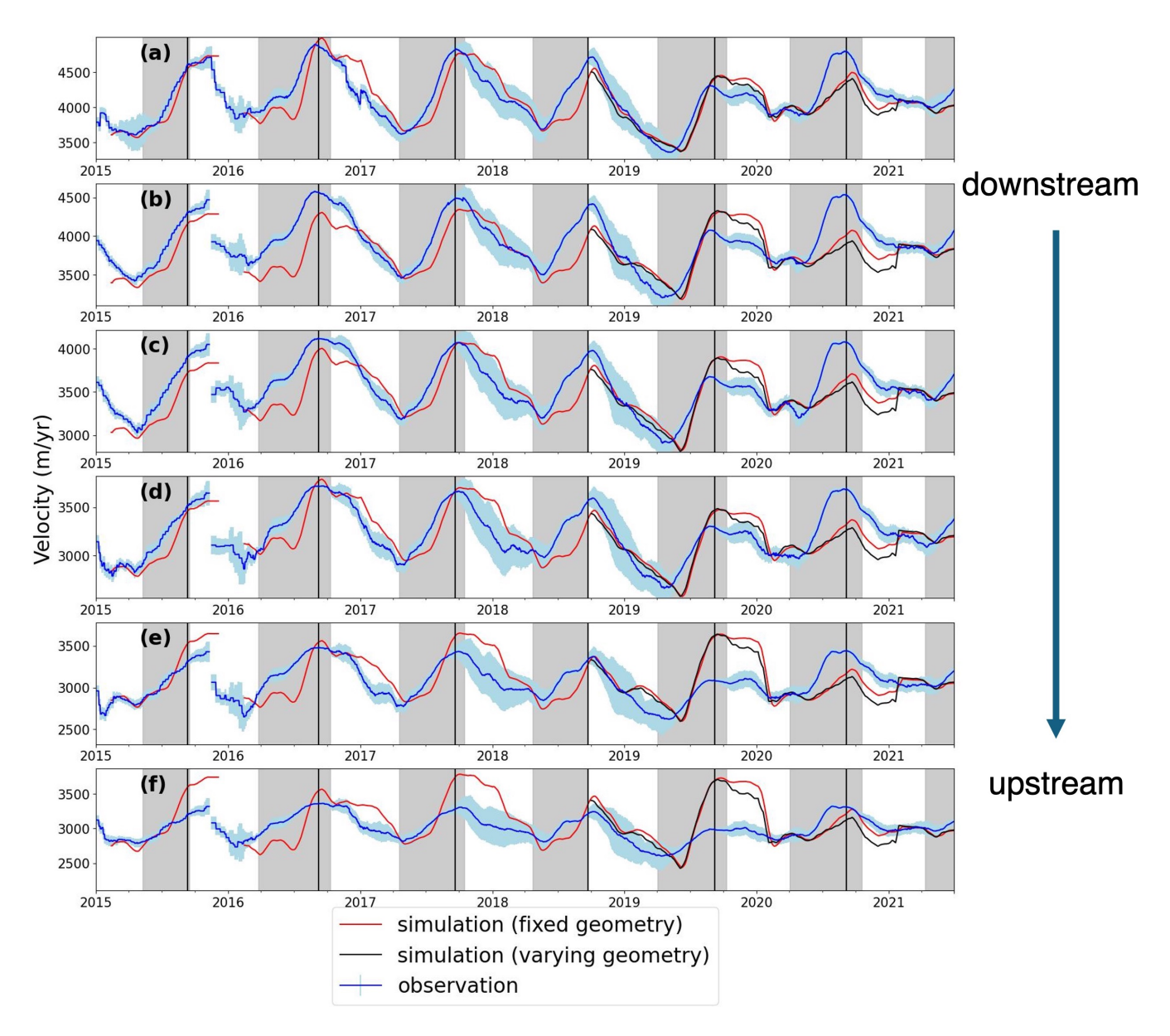


Figure S3. Velocity observations and simulations from downstream to upstream regions for KUJ.

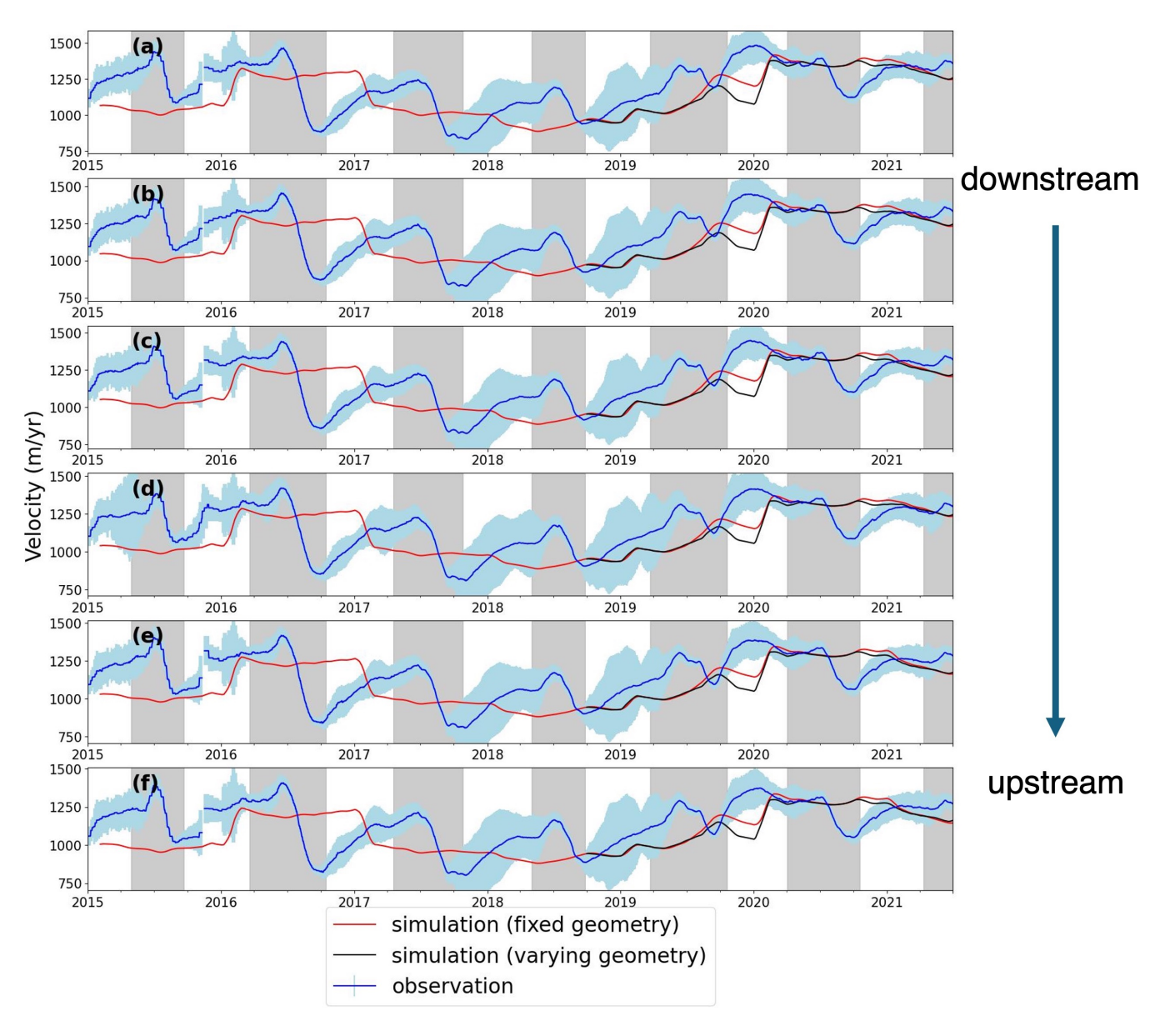


Figure S4. Velocity observations and simulations from downstream to upstream regions for KAN.

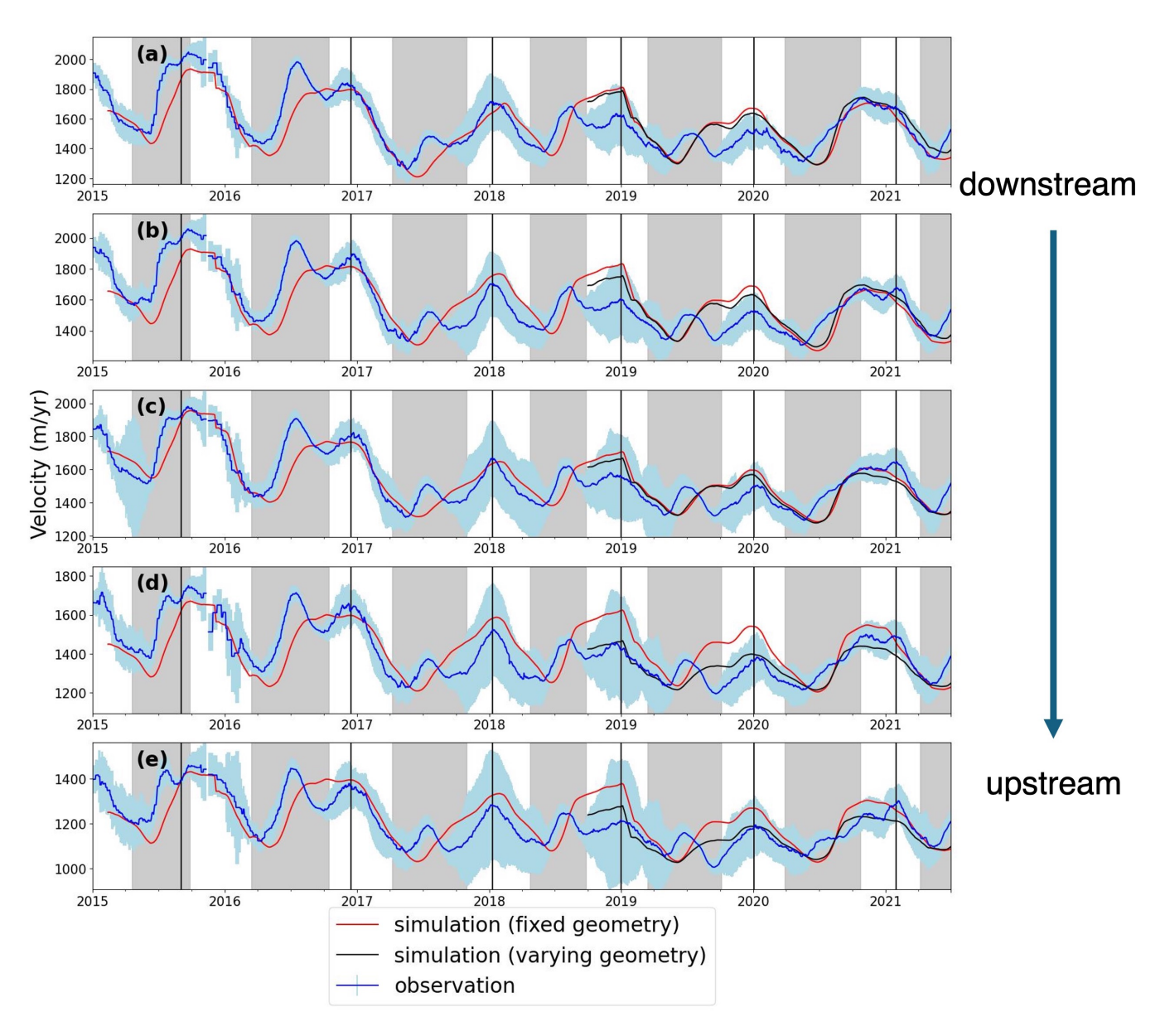


Figure S5. Velocity observations and simulations from downstream to upstream regions for EQP.

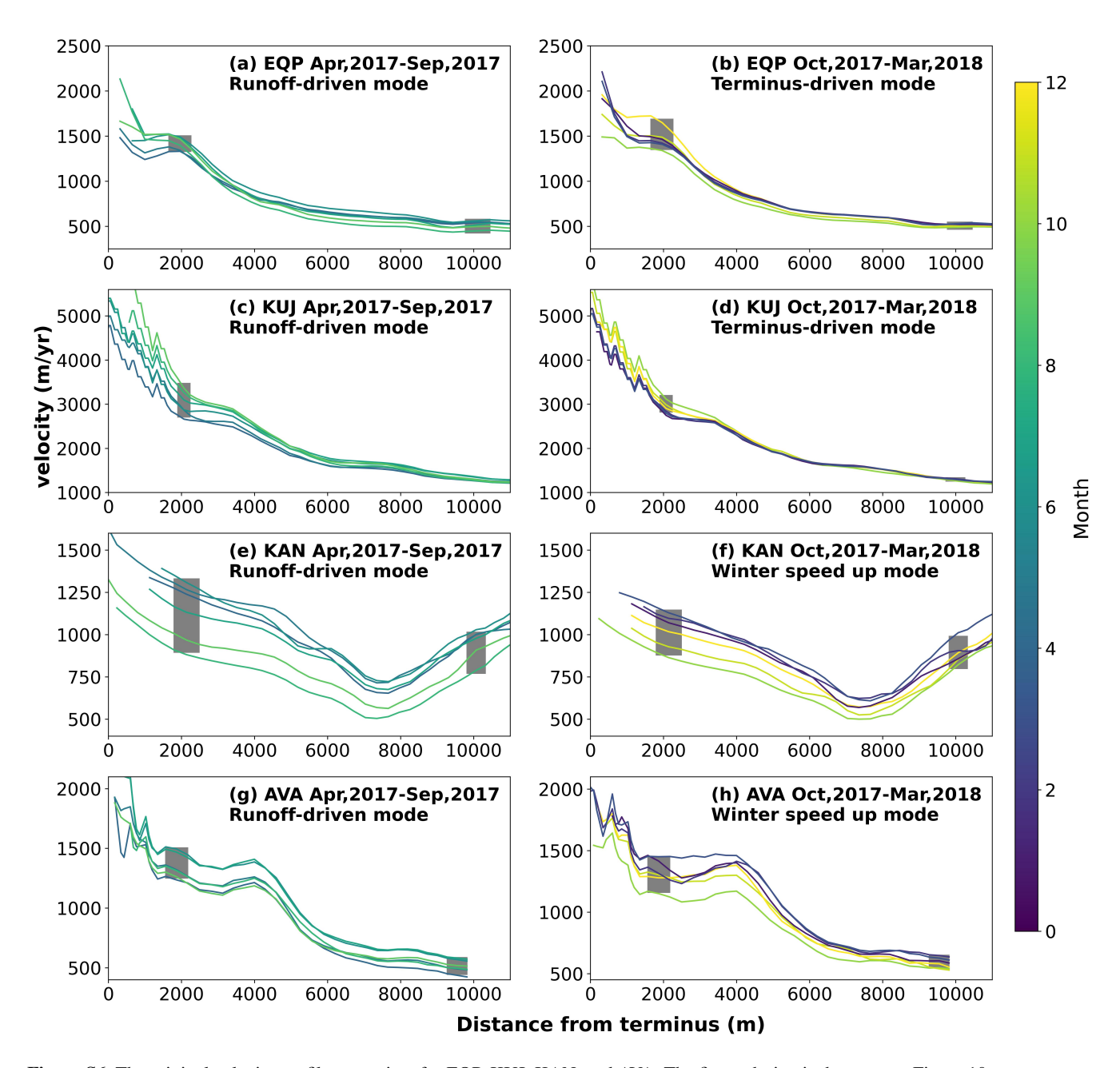


Figure S6. The original velocity profiles over time for EQP, KUJ, KAN, and AVA. The figure design is the same as Figure 10.

References

115

120

- Felikson, D., Bartholomaus, T. C., Catania, G. A., Korsgaard, N. J., Kjær, K. H., Morlighem, M., Noël, B., Van Den Broeke, M., Stearns, L. A., Shroyer, E. L., et al.: Inland thinning on the Greenland ice sheet controlled by outlet glacier geometry, Nature Geoscience, 10, 366–369, https://doi.org/10.1038/ngeo2934, 2017.
 - Felikson, D., A. Catania, G., Bartholomaus, T. C., Morlighem, M., and Noël, B. P. Y.: Steep Glacier Bed Knickpoints Mitigate Inland Thinning in Greenland, Geophysical Research Letters, 48, e2020GL090112, https://doi.org/https://doi.org/10.1029/2020GL090112, 2021.
- 110 Medley, B., Neumann, T. A., Zwally, H. J., Smith, B. E., and Stevens, C. M.: Simulations of firn processes over the Greenland and Antarctic ice sheets: 1980–2021, The Cryosphere, 16, 3971–4011, https://doi.org/10.5194/tc-16-3971-2022, 2022.
 - Porter, C., Morin, P., Howat, I. M., Noh, M.-J., Bates, B., Peterman, K., Keesey, S., Schlenk, M., Gardiner, J., Tomko, K., Willis, M. J., Kelleher, C., Cloutier, M., Husby, E., Foga, S., Nakamura, H., Platson, M., Wethington, M. J., Williamson, C. J., Bauer, G., Enos, J., Arnold, G., Kramer, W., Becker, P., Doshi, A., D'Souza, C., Cummens, P., Laurier, F., and Bojesen, M.: ArcticDEM Strips (Version 4.1), https://doi.org/10.7910/DVN/C98DVS, 2022.
 - Smith, B., Dickinson, S., Jelley, B. P., Neumann, T. A., Hancock, D., Lee, J., and Harbeck., K.: ATLAS/ICESat-2 L3B Annual Land Ice Height, Version 3, https://doi.org/10.5067/ATLAS/ATL11.003, 2021.
 - Smith, B., Adusumilli, S., Csathó, B. M., Felikson, D., Fricker, H. A., A. Gardner, N. H., J. Lee, J. N., Paolo, F. S., Siegfried, M. R., Sutterley, T., and the ICESat-2 Science Team.: ATLAS/ICESat-2 L3A Land Ice Height, Version 6, https://doi.org/10.5067/ATLAS/ATL06.006, 2023a.
 - Smith, B., Sutterley, T., Dickinson, S., Jelley, B. P., Felikson, D., Neumann, T. A., Fricker, H. A., Gardner, A., Padman, L., Markus, T., Kurtz, N., Bhardwaj, S., Hancock, D., and Lee., J.: ATLAS/ICESat-2 L3B Gridded Antarctic and Arctic Land Ice Height Change, Version 3, https://doi.org/10.5067/ATLAS/ATL15.003, 2023b.